
Proceedings Paper:
Evans, M., Du, J., Cao, L. et al. (2025) Robotic colonoscopy: can high fidelity simulation optimize robot design and validation? In: 2025 IEEE International Conference on Robotics and Automation (ICRA). 2025 IEEE International Conference on Robotics and Automation (ICRA), 19-23 May 2025, Atlanta, GA, USA. Institute of Electrical and Electronics Engineers (IEEE), pp. 2954-2960. ISBN: 9798331541408.

https://doi.org/10.1109/icra55743.2025.11128805

Robotic Colonoscopy: Can high fidelity simulation optimize robot design and validation?

M. Evans, J. Du, L. Cao, S. Dogramadzi[1]

Abstract— **This paper presents the use of a simulation environment as an accurate, ethical and sustainable alternative to testing robotic prototypes in animal models and simplified phantom models, specifically developed for robotic colonoscopy devices inside the human colon. A virtual simulation of the locomotion mechanism of a prototype robotic colonoscope and the colon was created in Ansys, and robot/colon experiments were conducted on different colon surfaces to validate simulation results. The successfully simulated propulsion force generated by the prototype produced an RMSE of 7% when compared at the optimal operating condition of the device, and 25-30% when compared to a full range of device velocities. The larger RMSE is due to physical phenomena that were not present in the simulation due to the constraints applied. The simulation, however, allowed evaluation of difficult quantities to measure in the real settings such as the normal interaction force between the device and tissue wall, and stress distribution across the locomotion mechanism, as well as a phenomenon of oscillating propulsion force resulting from the device design. This work demonstrates feasibility of using finite element simulation to shape the design and optimization of a robotic colonoscope, and understands its interaction with highly complex human anatomy.**

I. Introduction

Colorectal cancer (CRC) is the third most common cancer worldwide, with a recent estimate predicting a worldwide rise in incidence by 3.2 million, and mortality by 1.6 million, by the year 2040[1]. The gold standard screening technique for CRC is flexible colonoscopy[2], with a recent study estimating that colonoscopy screening patients experience a 31% reduction in risk of CRC, and a 50% reduction in CRC-related deaths[3]. Unfortunately, a stigma has arisen around the procedure, with around 60% of all CRC deaths being the result of patients avoiding screening due to discomfort/pain and embarrassment [4].

To alleviate some of this stigma, as well as improving the quality of endoscopic surgery (e.g. reducing time, increasing safety and efficacy[5]), robotic devices have been in development for many years. Such devices have included 'inchworm' locomotion[6,7], motor driven devices[8-10] and wireless capsule endoscopes [11,12]. There are also a number of commercially available flexible robotic colonoscopes, including NeoGuide, Invendoscope™ and Endotics System [13].

For such devices to be deemed functional and safe for use in a real human colon, testing should take place in an environment that is a realistic approximation of a human colon, incorporating the properties and structures seen in and around the organ, such as the abdominal wall, small intestine and mesocolon. To test devices in the past, studies have used in-vivo animal models, after which the animal is slaughtered [6,10], and solid test beds [6,7,12], sometimes incorporating ex-vivo colon tissue, but only demonstrating movement in a 2D plane rather than inside a 3D space.

We propose an alternative direction to assessing in-the-body robotic devices design to alleviate the use of unethical animal practices and crudely designed test rigs. An accurately modelled simulation environment with a human colon and its interactions with a prototyped robotic endoscopy device is presented in this paper that for the first time combines soft tissue modelling and an endoscopic robot physical test performance. Sustainability is an additional advantage of this approach which obviates the need to create iterative physical prototypes to optimise their functionality in high fidelity environments.

The use of virtual anatomy simulations in surgical and endoscopic clinical practice has increased with the advancement of computing hardware, for example to allow for remote surgical intervention as seen with the Nvidia Clara™ platform [14] and for education/training on dissection and endoscopy [15]. The colon has been simulated in some related works for different purposes. Lattice meshes have been used to simulate the deformation of the colon wall due to an endoscope for colonoscopy simulators [16,17,18], however these examples were limited by using a linear elastic mass-spring model as opposed to a nonlinear material model, and not modelling the tissue thickness [16,17], and by not simulating the deformation of the colon due to the interaction with the endoscope [18]. The accuracy of the material model and geometry, as well as the deformation due to the interaction with an internal device, are important factors in calculating accurate interaction forces between the two media.

[1] Michael Evans (email: maevans1@sheffield.ac.uk)
Jiayang Du (email: ddu4@sheffield.ac.uk)
Lin Cao (email: l.cao@sheffield.ac.uk)
Sanja Dogramadzi (s.dogramadzi@sheffield.ac.uk)
All authors are affiliated with:
School of Electronic and Electrical Engineering
The University of Sheffield, Sheffield, S1 3JD
United Kingdom

The finite element method (FEM) has also been used to model colon tissue. This has been done in different capacities, for example to simulate a small square section of mouse colon tissue using two [19] and three [20] layers with different material models to simulate the through-thickness heterogeneity of the tissue. While this creates an accurate model, it can only be applied to a small sample of tissue, due to a high computational burden involved with the intricacies of this simulation. Thus, this method cannot be used to simulate a device interacting with a larger section of colon.

Another example of a FEM simulation of the colon can be seen in a study of the transit of a capsule device through the intestinal contents [21]. While this does model some interaction between the device and the colon, it is mainly through an internal fluid and does not focus specifically on the device-wall interaction. Additionally, the locomotion method of the device does not depend on interaction forces with the colon wall, but is carried via the flow of intestinal contents.

An entire colon simulation using FEM to test the difference in interaction forces between the tissue and a colonoscope tip at different orientations was reported in [22]. When applied to a constrained tissue sample and the whole colon, the drastic difference in forces when comparing the two tissue states was demonstrated. The limitations of this study include the colon tissue simulation using a linear elasticity model and the colon geometry model assuming a cylindrical shape, simplifying its actual haustrated structure.

Other hollow organ tissues present in the human body have been simulated using FEM. The trachea was modelled to explore the effects of surgical intervention and scaffold-based interventions, with three types of tissue being modelled using a second order Ogden model [23]. This model assumes isotropic elasticity, and tissues in the trachea (and colon) exhibit anisotropic elasticity in reality. However, the isotropic assumption is suitable for tissues with minimal anisotropy, and can allow for less computational burden during FEM simulations.

Furthermore, the stomach has been modelled via FEM in multiple studies on bariatric surgery [24,25]. For the tissue model, constitutive equations were formulated and fitted to mechanical testing data of stomach tissue to find hyperelastic and viscoelastic material parameters. This provided an accurate description of the tissue's response to a gastric band and internal pressure distribution.

The contributions from this paper are as follows:

- An FEM simulation setup to analyse the performance of the locomotion mechanism of an endoscopic robot prototype, by simplifying the mechanism with approximations and constraints;
- Results of interaction parameters including the propulsion force of the device, for comparison with physical tests, and the normal force at the interaction and stress distribution, which were not obtainable in real life;
- Analysis of the simulation accuracy and comparison with measurements obtained from real life experiments with the robotic prototype;
- Discussion on advantages of the proposed simulation approach.

I. Simulation Design

A. *Simulation environment*

To simulate the locomotion mechanism of the device, Ansys(R) Mechanical 2023 R2 was used. A transient structural FEM simulation was set up. To simulate a soft tissue such as colon wall tissue, an existing material model within the Ansys library was used - VMQ silicone was chosen for its nonlinear elastic properties, similar to that of colon tissue, with a 3-parameter Mooney-Rivlin model for incompressible hyperelasticity:

$$\Psi = C_{10}(\bar{I}_1 - 3) + C_{10}(\bar{I}_2 - 3) + C_{10}(\bar{I}_1 - 3)(\bar{I}_2 - 3), \quad (1)$$

where Ψ is the strain energy; C_{10}, C_{01}, and C_{11} are material constants (32.45 kPa, -2.581 kPa and 6.687 kPa respectively); and $\bar{I}_1$ and $\bar{I}_2$ are the first and second invariants of the distortional part of the right Cauchy-Green stress tensor. For the friction between the prototype locomotion mechanism and the tissue wall, a linear coefficient of friction model was used. All FEM simulations were run using Dell PowerEdge R650 machines with Intel Xeon Platinum 8358 CPUs, run on 32 cores in shared-memory parallel.

B. *Endoscopic robot prototype*

The endoscopic robot prototype simulated in this study is the device published in [26], and can be seen in Fig. 1. A motor-driven worm gear inside the device interlocks with treads made from silicone rubber (SmoothSil 960) to transmit the propulsion force from an external motor via a flexible shaft. The ratio of tread linear velocity to worm gear angular velocity is 13mm to 1 rotation. It uses four sets of bellows and struts, which can expand and contract to adaptively maintain traction along a colonic tract of varying diameter, as shown in Fig. 2.

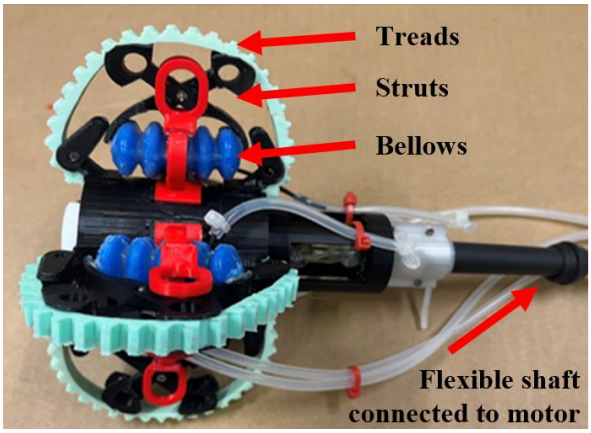

Figure 1. The robotic prototype uses four bellows to independently control four tracks for locomotion and diameter adaptation along the colon wall.

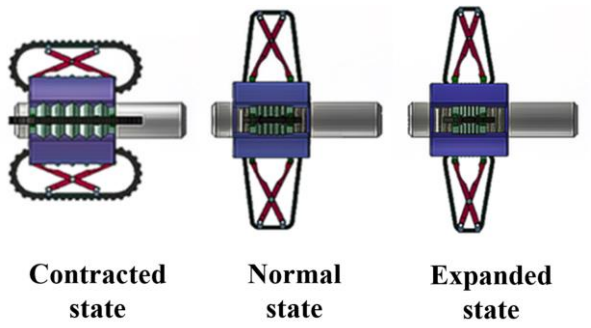

Figure 2. To decrease the diameter of the device, the bellows pressure is increased, widening the struts and moving the track inwards. To increase the diameter of the device, bellows pressure is decreased, narrowing the struts and moving the track outwards.

The nominal track-to-track diameter of the prototype is 140 mm (a 4:1 scale of the device in practice), but subject to the activation of the expansion mechanism, the diameter of the prototype can change by almost 53%, from 99.6 mm to 151.6 mm.

C. *Physical validation experiments*

Due to the high number of moving parts in the device, and the nonlinearities associated with the material properties of the device treads and soft tissue, multiple simplifications were made to the device in the simulation environment:

1. Only one out of the four sets of struts was simulated to reduce the number of elements by four and shorten the simulation time.
2. The struts were modelled as a single object with two circular points of contact to match the geometry of the strut tips when at resting point, and decrease the number of contact objects required.
3. Due to the above, the bellows were not simulated, instead using a direct displacement constraint to control how far the struts extend or retract
4. The treads were modelled as a strip rather than a continuous loop, so that less intense deformation would occur to the mesh elements, allowing for easier convergence in the simulation.
5. The tissue surface was modelled as an 8mm wide strip (the same as the tracks), with the outside edge fixed in place and the sides constrained not to deform in the y-direction (see Fig. 3).

The colon and device simulation setup can be seen in Fig. 3. The tread object was placed in contact with the tissue wall, by applying a displacement to the strut object, and accelerated up to 5 different velocities: 16.25 mm/s, 26 mm/s, 32.5 mm/s, 43.3 mm/s and 65 mm/s. These values correspond to worm gear angular velocities of 75 rpm, 120 rpm, 150 rpm, 200 rpm and 300 rpm, respectively, calculated using the conversion of 1 worm gear rotation to 13mm of track movement. The simulation took place in 3 time steps: the displacement of the struts to push the tread into the tissue wall (0-1.5s); the acceleration of the tread (1.5-2s); and the movement of the tread at full speed (2-3s).

The beam object has been implemented as a method to determine the propulsion force, by calculating the force applied to the beam in the z-direction as a result of the contact between the tracks and the tissue wall. To maintain rigidity, it was modelled as structural steel, with a 50 mm length and 2 mm radius. The input variables include a displacement applied to the strut tips and a relative velocity between the tread and the reference core object (Fig. 3 d). The output variables are the displacement/deformation and von-Mises stress of the tread, the normal force at the interaction between the strut and the treads, and the frictional force between the tread and the tissue wall - this was multiplied by four to calculate the total propulsion force for the full device. The Smooth-Sil 960 silicone used for the treads was modelled with an incompressible 5-parameter Mooney-Rivlin hyperelastic model:

$$\Psi = C_{10}(\bar{I}_1 - 3) + C_{01}(\bar{I}_2 - 3) + C_{10}(\bar{I}_1 - 3)(\bar{I}_2 - 3) + C_{20}(\bar{I}_1 - 3)^2 + C_{02}(\bar{I}_2 - 3)^2, \square 2\square$$

where all the nomenclature is the same as equation (1) with two further material constants, C_{20} and C_{02}. The material constants are defined as -1.239 MPa, 1.83 MPa, -10.14 MPa, 6.005 MPa and 4.782 MPa respectively [27].

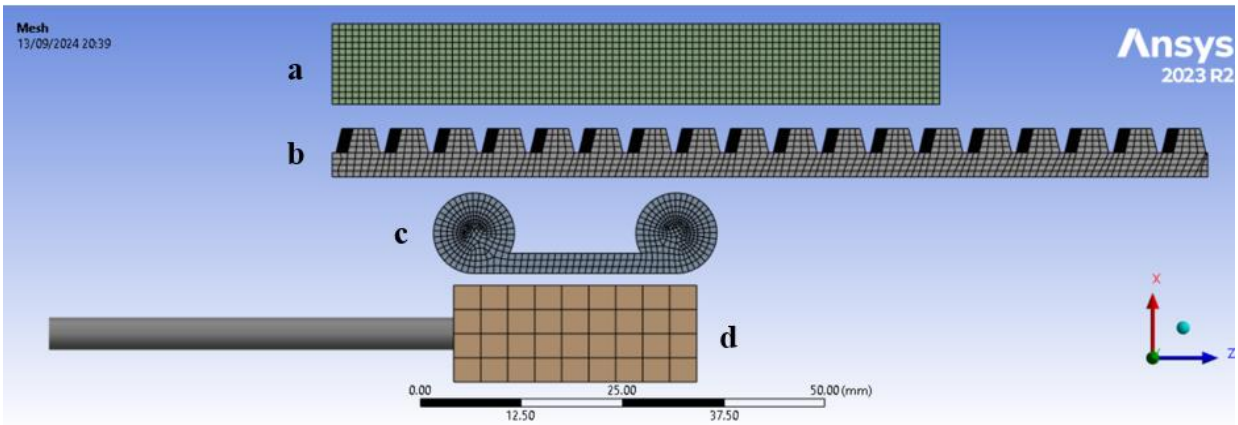

Figure 3. The simplified device used for the simulation setup, where **a** approximates the tissue wall, **b** approximates the device treads, **c** approximates the device struts and **d** acts as a reference for the core of the device. Image courtesy of Ansys Inc.

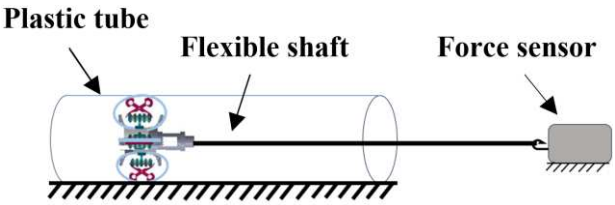

Figure 4. The physical setup for measuring the propulsion force of the device.

A contact object was set up between the tread and tissue wall with a linear coefficient of friction model, using 0.4 for a bowel tissue wall [28] and 0.2 for a plastic pipe surface [29]. A frictionless contact object was set up between the strut tips and the tread, and a pure-penalty contact detection method (program controlled) was used for both contact objects.

D. Physical validation experiments

To test the effectiveness of the robot locomotion, the propulsion force was measured at different worm gear rotational velocities, and using different surface materials. As shown in Fig. 4, the device was placed inside a hollow plastic tube, and tested on the tube surface and with an artificial bowel tissue surface with a thickness of 9mm [30]. To measure the propulsion force, an inextensible string was fixed between the flexible shaft and a force sensor (LSb201, FUTEK, USA), acting as a medium for the force measurement. The bellows were closed off at atmospheric pressure, ensuring that there was sufficient normal force between the treads and the tube for locomotion.

II. RESULTS

A. FEM simulation

The simulation results of propulsion force vs motor velocity can be seen in Fig. 5. The calculated propulsion forces were nearly independent of the tread velocity, the largest difference being around 0.15N across the results from the tests

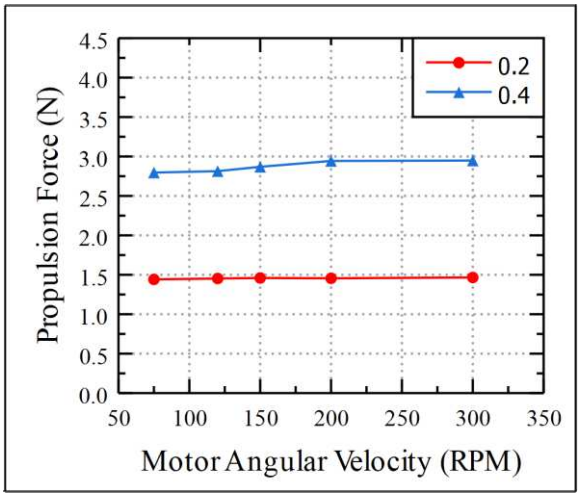

Figure 5. Results from the simulation, aimed to predict the propulsion force at different worm gear speeds. The coefficient of friction between the tread and the tissue wall was 0.4 (black) and 0.2 (red), representing the artificial bowel tissue and plastic pipe wall respectively

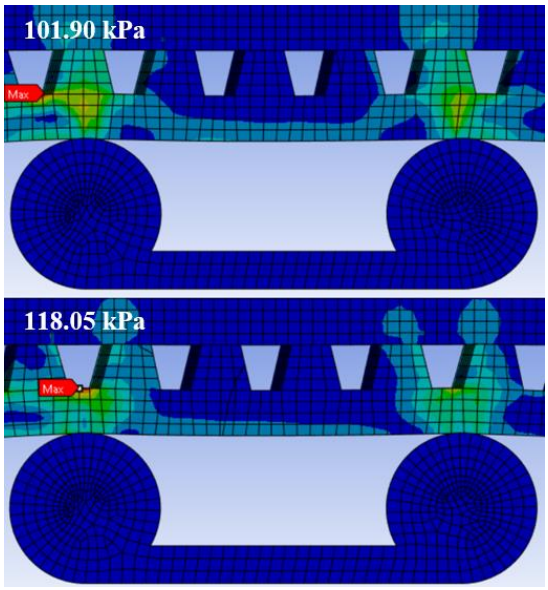

Figure 6. The stress distribution of the treads and tissue wall during the second simulation scenario. For the high force producing state (top), the maximum stress calculated was lower than that in the low force producing state (bottom).

using a coefficient of friction of 0.4. These results had a sinusoidal relationship between time and propulsion force, and the average values at the full speeds were taken as the resulting force. The reasoning for this is due to the spacing of the strut tips and the spacing of the tread teeth coinciding, creating essentially high and low force producing states. This is demonstrated in Fig. 7 and is discussed further in section IV.

Another quantity measured in the simulations was the stress distribution of the track, shown in Fig. 6. The maximum stress oscillated similarly to the interaction forces, however the stress in the tread was higher during lower force producing states.

The stress was analysed at the locations of the track that were directly above the strut tips, at the high and low force producing states during the third time step of the 150 rpm simulation - this speed was chosen because it allowed for the most data points without the end of the tread object raising the stress in the tread as it approached the strut. This can be seen at the start of the results for the rear (left) strut tip and slightly towards the end of the results for the front (right) strut tip.

At the front tip, plotted in Fig. 8, the average stress was 64.6 kPa during the high force producing state, and 109 kPa during the low force producing state. At the rear tip, plotted in Fig. 9, the average stresses were 60.2 kPa and 92.5 kPa respectively. The stress values levelled out when both ends of the tread were around 40mm away from either strut tip, at 57.6 kPa for the high force producing state and 88.7 kPa for the low force producing state.

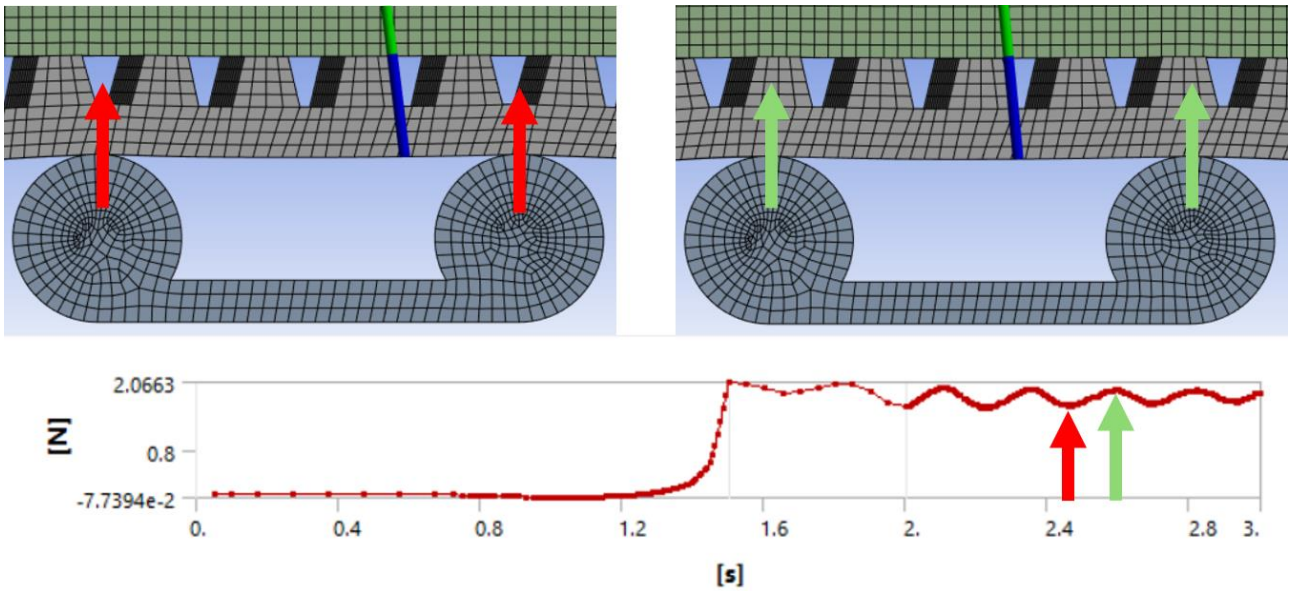

Figure 7. The simulated mechanism in its low force producing state (left), its high force producing state (right) and a graph of the normal force vs time showing the mentioned oscillation of the force, with indicators on where the two snapshots take place within the timeframe of the simulation (bottom). The low force occurs when the strut tips line up with the gaps between the tread teeth, and the high force occurs when the strut tips line up with the tread teeth.

B. Physical validation experiments

The results from the propulsion force experiments show an optimal worm gear rotational velocity of ~150 rpm (Fig. 10). At speeds lower than this, the device does not generate sufficient traction force. Above this value, the transmission efficiency of the flexible shaft declines, which consequently affects the coupling between the worm gear and treads, leading to tread slippage. Because of these factors, the RMSE of propulsion force between the experimental and simulation results on the smooth tube surface is 0.313 N (25.8%), and on the tissue surface is 0.703 N (29.6%) when compared to the full range of motor velocities, but when compared to the peak propulsion force in either state, the RMSE is only 0.092 N (7.6%) and 0.162 N (6.8%) for the smooth tube and tissue surfaces, respectively. The stress distribution across the treads was not measurable in the physical experiments.

III. Discussion

The FEM simulations were able to compute the same propulsion force measured in the real world prototype experiments at optimal prototype velocity - ~3N for the bowel tissue, and ~1.5N for the plastic surface. This proves that the simulation environment was suitable to measure the interaction force between the bowel tissue and the device - a quantity that is difficult to measure in the real world, and important in terms of assessing device performance and safety.

While the FEM results show an accurate calculation of the propulsion force at an optimal velocity, the real world results differ in the overall trend between the two variables. This is due to the constraints applied to the simulation model. Effectively a quarter of the full device is modelled, which has

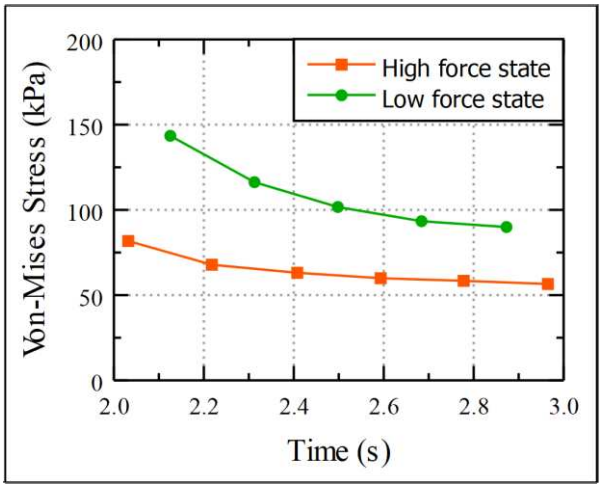

Figure 8. A plot of the stress measured in the tread above the rear strut tip (left hand side in Fig. 6) during the third time step of the 150 rpm simulation.

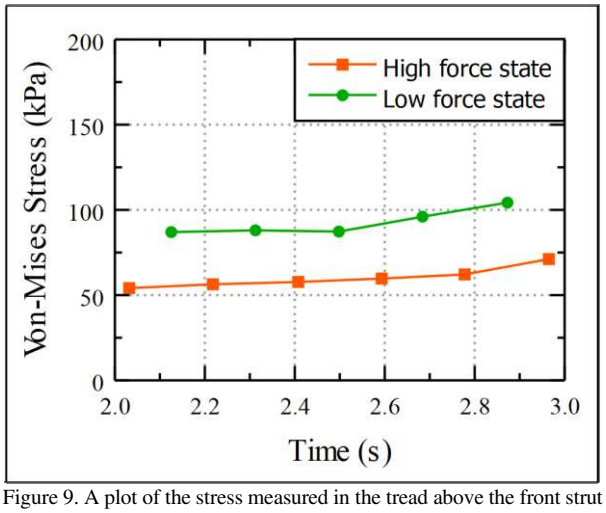

Figure 9. A plot of the stress measured in the tread above the front strut tip (right hand side in Fig. 6) during the third time step of the 150 rpm simulation.

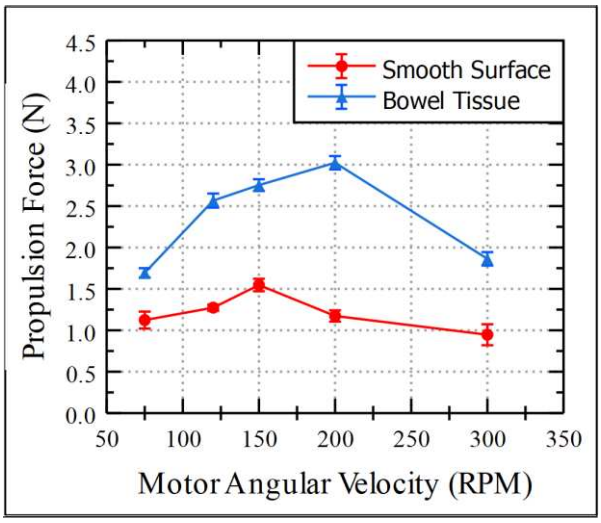

Figure 10: A graph showing the results of the physical experiments at different rotational velocities of the worm gear for the smooth surface and tissue surface cases.

led to constraints being applied to the 'core' object to constrain it to only move along one axis, thereby not being able to simulate the unsteady movement of the device, especially at high speeds. Furthermore, because the velocity is applied as a linear relationship between the treads and the core, the torque from the worm gear is also not simulated. This torque has a large effect on the locomotion of the real world prototype, as at higher motor speeds, the torque increases to levels which make the device unstable within the tube, reducing the propulsion force achieved.

As well as approximations made when modelling the device, approximations were made in the relationships between moving parts. A linear coefficient of friction model was used for the contact between the treads and the tissue wall, thereby not being able to model the velocity-dependent frictional force seen in the experimental results. Finally, the results for the frictional force between the tread and the tissue wall had an error margin of ±5% of the amplitude of the oscillating force measurement, due to a high convergence tolerance needed for the simulations to complete. This is a relatively minor shortcoming that was mitigated by averaging the oscillating forces.

Despite these limitations, the simulation does have some advantages over the real world experiments. This can be seen in the oscillating frictional force calculated between the treads and tissue wall, demonstrated in Fig. 7. This occurs due to the distance between the strut tips being very close to a multiple of the distance between the tread teeth, and is not something that could be observed in real world experiments due to the small size of the tread parts.

The simulation found this issue, and can measure how much it affects the frictional force - in this scenario, the largest amplitude in the frictional force calculation was around 0.2N, or roughly 25% of the average frictional force value at each tread. This indicates that the component should be redesigned to allow for optimal propulsion force generation.

Another quantity that cannot be measured directly in the real world, and would be difficult to estimate accurately due to the small size of the treads, is the stress distribution visualised in Fig. 6. The stress measurement was slightly impeded by the constraint applied to the ends of the tread, to ensure that the only point of contact between the tread and tissue wall was adjacent to the strut tips, as would be the case with the tread in the real device. The simulation environment offers a way to visualise the locations of stress concentrations in the treads, allowing for the ability to design different kinds of treads to minimise the concentrations and magnitudes of stress, without having to create physical prototypes. In this particular case, the average maximum stress during the third time step of the simulation was 112 kPa, which is only 2.5% of the tensile strength of the tread material [31], indicating that no optimisation is necessary in this regard.

Following these experiments, the simulation environment can thus be used to optimise the geometry of the locomotion mechanism, repeating tests to find a layout that can mitigate the loss in propelling force.

IV. Conclusion

While the simulation at this stage did not perfectly model the real world device, it was able to calculate the propulsion force generated in the optimal scenario, just by modelling a quarter of the device, and it was able to find a phenomenon that occurred due to the layout of the parts in the device's locomotion mechanism, thereby allowing for the mechanism to be redesigned for a more optimal force output.

Further work is planned to include the whole device in the simulation and collect the same parameters for evaluation. As well as this, we are planning to improve the simulation models by utilising a large set of physical test data to improve the colon physical model and reduce the gap with real world results. By being able to better predict the real-life behaviour of developmental devices, unethical and inaccurate testing solutions can be significantly reduced.

Acknowledgment

This work was in part supported by a doctoral scholarship for the first author from the School of Electrical and Electronic Engineering at the University of Sheffield.

References

[1] E. Morgan et al., "Global burden of colorectal cancer in 2020 and 2040: incidence and mortality estimates from GLOBOCAN," Gut, vol. 72, no. 2, p. gutjnl-2022-327736, Sep. 2022, doi: https://doi.org/10.1136/gutjnl-2022-327736.

[2] M. B. Nierengarten, "Colonoscopy remains the gold standard for screening despite recent tarnish," Cancer, vol. 129, no. 3, pp. 330–331, Jan. 2023, doi: https://doi.org/10.1002/cncr.34622.

[3] M. Bretthauer et al., "Effect of Colonoscopy Screening on Risks of Colorectal Cancer and Related Death," New England Journal of Medicine, vol. 387, no. 17, Oct. 2022, doi: https://doi.org/10.1056/nejmoa2208375.

[4] G. Ciuti et al., "Frontiers of Robotic Colonoscopy: A Comprehensive Review of Robotic Colonoscopes and Technologies," Journal of

Clinical Medicine, vol. 9, no. 6, p. 1648, May 2020, doi: https://doi.org/10.3390/jcm9061648.
[5] I. Boškoski and G. Costamagna, "Endoscopy robotics: Current and future applications," Digestive Endoscopy, vol. 31, no. 2, pp. 119–124, Oct. 2018, doi: https://doi.org/10.1111/den.13270.
[6] Byung Kyu Kim, Hun Young Lim, Jong Hyeon Park, and J.-O. Park, "Inchworm-Like Colonoscopic Robot with Hollow Body and Steering Device," Jsme International Journal Series C-mechanical Systems Machine Elements and Manufacturing, vol. 49, no. 1, pp. 205–212, Jan. 2006, doi: https://doi.org/10.1299/jsmec.49.205.
[7] P. Dario, M. C. Carrozza, and A. Pietrabissa, "Development and in Vitro Testing of a Miniature Robotic System for Computer-Assisted Colonoscopy," Computer Aided Surgery, vol. 4, no. 1, pp. 1–14, Jan. 1999, doi: https://doi.org/10.3109/10929089909148154.
[8] C. D. Sheerer, D. Drozek, and J. Choi, "A Hand-Held Device for Controlling a Mounted, Motor Driven Colonoscope1," Journal of Medical Devices, vol. 9, no. 3, Sep. 2015, doi: https://doi.org/10.1115/1.4030601.
[9] D. Kim, D. Lee, S. Joe, B.-I. Lee, and B. Kim, "The flexible caterpillar based robotic colonoscope actuated by an external motor through a flexible shaft," Journal of mechanical science and technology, vol. 28, no. 11, pp. 4415–4420, Nov. 2014, doi: https://doi.org/10.1007/s12206-014-1009-2.
[10] T. Rösch et al., "A motor-driven single-use colonoscope controlled with a hand-held device: a feasibility study in volunteers," Gastrointestinal Endoscopy, vol. 67, no. 7, pp. 1139–1146, Jun. 2008, doi: https://doi.org/10.1016/j.gie.2007.10.065.
[11] S. Yim and M. Sitti, "Design and analysis of a magnetically actuated and compliant capsule endoscopic robot," in 2011 IEEE International Conference on Robotics and Automation, Shanghai, China, 2011, pp. 4810–4815. Accessed: Sep. 10, 2024. [Online]. Available: https://doi.org/10.1109/ICRA.2011.5979819
[12] J. Zhang, Y. Liu, J. Tian, D. Zhu, and S. Prasad, "Design and Experimental Investigation of a Vibro-Impact Capsule Robot for Colonoscopy," IEEE robotics and automation letters, vol. 8, no. 3, pp. 1842–1849, Mar. 2023, doi: https://doi.org/10.1109/lra.2023.3243804.
[13] F. Cosentino et al., "Robotic Colonoscopy", Colonoscopy. InTech, Aug. 29, 2011. doi: 10.5772/20428.
[14] NVIDIA Corporation, "NVIDIA Clara for Medical Devices," NVIDIA, 2024. https://www.nvidia.com/en-us/clara/medical-devices/# (accessed Sep. 15, 2024).
[15] K. Kwon, J. S. Park, and B.-S. Shin, "Virtual Anatomical and Endoscopic Exploration Method of Internal Human Body for Training Simulator," Journal of Korean Medical Science, vol. 35, no. 12, Jan. 2020, doi: https://doi.org/10.3346/jkms.2020.35.e90.
[16] H. Jung, Doo Yong Lee, and W. Ahn, "Real-time deformation of colon and endoscope for colonoscopy simulation," International Journal of Medical Robotics and Computer Assisted Surgery, vol. 8, no. 3, pp. 273–281, Feb. 2012, doi: https://doi.org/10.1002/rcs.1414.
[17] T. Wen, D. Medveczky, J. Wu, and J. Wu, "Colonoscopy procedure simulation: virtual reality training based on a real time computational approach," BioMedical Engineering OnLine, vol. 17, no. 1, Jan. 2018, doi: https://doi.org/10.1186/s12938-018-0433-4.
[18] Lucas Zanusso Morais et al., "An enhanced interactive endoscope model based on position-based dynamics and Cosserat rods for colonoscopy simulation," Computers & Graphics, vol. 116, pp. 345–353, Nov. 2023, doi: https://doi.org/10.1016/j.cag.2023.08.020.
[19] Y. Zhao, S. Siri, B. Feng, and D. M. Pierce, "Computational Modeling of Mouse Colorectum Capturing Longitudinal and Through-thickness Biomechanical Heterogeneity," Journal of the Mechanical Behavior of Biomedical Materials, vol. 113, p. 104127, Jan. 2021, doi: https://doi.org/10.1016/j.jmbbm.2020.104127.
[20] Y. Zhao, B. Feng, and D. M. Pierce, "Predicting the micromechanics of embedded nerve fibers using a novel three-layered model of mouse distal colon and rectum," Journal of the Mechanical Behavior of Biomedical Materials, vol. 127, p. 105083, Mar. 2022, doi: https://doi.org/10.1016/j.jmbbm.2022.105083.
[21] P. G. Kalozoumis, M. Marino, E. L. Carniel, and D. K. Iakovidis, "Towards the Development of a Digital Twin for Endoscopic Medical Device Testing," Studies in systems, decision and control, pp. 113–145, Jan. 2022, doi: https://doi.org/10.1007/978-3-030-96802-1_7.
[22] M. Evans and S. Dogramadzi, "A computational model of the human colon for use in medical robotics," AIP advances, vol. 14, no. 2, Feb. 2024, doi: https://doi.org/10.1063/5.0179544.
[23] F. Safshekan, M. Tafazzoli-Shadpour, M. Abdouss, M. B. Shadmehr, and F. Ghorbani, "Finite element simulation of human trachea: Normal vs. surgically treated and scaffold implanted cases," International Journal of Solids and Structures, vol. 190, pp. 35–46, May 2020, doi: https://doi.org/10.1016/j.ijsolstr.2019.10.021
[24] Emanuele Luigi Carniel et al., "A biomechanical approach to the analysis of methods and procedures of bariatric surgery," Journal of Biomechanics, vol. 56, pp. 32–41, May 2017, doi: https://doi.org/10.1016/j.jbiomech.2017.02.029.
[25] C. G. Fontanella et al., "Computational Models for the Mechanical Investigation of Stomach Tissues and Structure," Annals of Biomedical Engineering, vol. 47, no. 5, pp. 1237–1249, Feb. 2019, doi: https://doi.org/10.1007/s10439-019-02229-w.
[26] Du, J., Cao, L., & Dogramadzi, S. (2024). Adaptable, shape-conforming robotic endoscope. Manuscript submitted to arXiv.
[27] Widmaier, N., Raps, L. (2023). Analysis of New Concepts for the Consolidation Roller in Laser-Assisted Automated Tape Placement Processes. In: Kiefl, N., Wulle, F., Ackermann, C., Holder, D. (eds) Advances in Automotive Production Technology – Towards Software-Defined Manufacturing and Resilient Supply Chains. SCAP 2022. ARENA2036. Springer, Cham. https://doi.org/10.1007/978-3-031-27933-1_26
[28] D. Accoto et al., "Measurements of the frictional properties of the gastrointestinal tract," in Proceedings of the 2nd AIMETA International Tribology Conference, 2001.
[29] C. Maier and T. Calafut, Polypropylene. William Andrew, 1998.
[30] LifeLike BioTissue, "Tissue Sheet Selector – LifeLike BioTissue," Lifelikebiotissue.com, 2021. https://lifelikebiotissue.com/shop/custom/tissue-sheet-selector (accessed Sep. 15, 2024).
[31] Smooth-On, Inc., "Smooth-SilTM 960 Product Information," Smooth-On, Inc., 2024. https://www.smooth-on.com/products/smooth-sil-960/ (accessed Sep. 15, 2024).